Journal of Molecular Graphics and Modelling 38 (2012) 220–225

Contents lists available at SciVerse ScienceDirect

Journal of Molecular Graphics and Modelling

journal homepage: www.elsevier.com/locate/JMGM

First principle investigation of transport properties of Lindqvist derivatives based molecular junction

Shizheng Wen[a], Wei Guan[a], Zhongmin Su[a,*], Likai Yan[a], Stefano Sanvito[b,*]

[a] Institute of Functional Material Chemistry, Faculty of Chemistry, Northeast Normal University, Changchun 130024, People's Republic of China
[b] School of Physics and CRANN, Trinity College, Dublin 2, Ireland

ARTICLE INFO

Article history:
Accepted 22 May 2012
Available online 12 June 2012

Keywords:
Lindqvist
Polyoxometalates
Carbon nanotube
Density functional theory (DFT)
Non-equilibrium Green's function (NEGF)
Quantum tunneling

ABSTRACT

The transport properties of Lindqvist type-polyoxometalates $H_2M_6O_{19}$ (M = Mo, W) sandwiched between carbon nanotube electrodes are investigated by using density functional theory combined with the non-equilibrium Green's function method. It is found that the precise position of the protonation has little effect on the transport properties of $H_2Mo_6O_{19}$, as it is established by investigating two different geometries. Furthermore we have discovered that $H_2Mo_6O_{19}$ and $H_2W_6O_{19}$ display similar conduction profiles with the main conduction mechanism being quantum tunneling. With a large energy gap and robust structural stability these molecules appear to be good candidate for high bias applications.

1. Introduction

Since the early theoretical predictions of Aviram and Ratner [1] and the pioneering experimental work of Reed et al. [2], molecular electronics has received increasingly large attentions as potential technology for constructing novel electronic devices. Numerous experimental and theoretical works have focused on devising and exploring new molecular junctions aimed at replacing with conventional electronic components, and many progresses have been made both from the experimental and the theoretical point of view [3–18]. Ab initio parameter-free modeling has played a pivotal role in this development as it offers a direct microscopic insight into the properties of the various molecular junctions. At present, there are two general theoretical strategies to tackle the quantum transport problem. The first focuses on the time-dependent transport properties of a nanodevice by using time-dependent density functional theory (TDDFT) [19–28]. In contrast, the second aims at exploring the steady state only and it is based on ground-state DFT. A practical implementation of the non-equilibrium Green's function (NEGF) scheme for quantum transport combined with DFT, that is the so-called DFT + NEGF approach, is the most popular choice for this second theoretical strategy [9–15]. Such a scheme is also used here.

One of the primary goals of molecular electronics is that of designing stable, reproducible and functional vertical molecular systems, whose assembly can be controlled at the nanoscale. Importantly, even under low bias voltage conditions huge current densities may be expected to travel through such molecules [28], thus undermining the structural stability of the molecular device. It is then important to construct new molecular complexes that can sustain such large current densities without significant structural deformations. Compounds including transition metal atoms may represent a good candidate to this goal.

In this work we consider a class of inorganic compounds, polyoxometalates (POMs), made primarily of oxygen and early transition-metal atoms, that can be employed as soluble molecular semiconducting oxides [29]. Even though the main interest for these molecular systems is in the field of catalysis, many other potential applications such as electrochemical displays, chemical sensors, capacitors, memory, and electrochemical cells have all been proposed [30–33]. POMs have one important characteristic, namely that they can accept one or more electrons without undergoing significant structural changes. Furthermore these additional electrons can delocalize over several metal centers within the molecular framework [34]. POMs can also be characterized as zero-dimension semiconductors [35]. To date the transport properties of this vast class of molecules have been extensively investigated in experiments designed around POM embedded in polymetric matrices or thin films [30,32,35–38]. To the best of our knowledge however there is no investigation available of the electronic transport through POMs at the single molecular level, although this can certainly contribute to the understanding of the electron transfer process in such compounds.

* Corresponding authors. Tel.: +86 431 8509 9108; fax: +86 431 8568 4009.
E-mail addresses: zmsu@nenu.edu.cn (Z. Su), sanvitos@tcd.ie (S. Sanvito).

1093-3263/$ – see front matter © 2012 Elsevier Inc. All rights reserved.
http://dx.doi.org/10.1016/j.jmgm.2012.05.005

Table 1
Reference configuration and cutoff radii for the pseudopotentials used in this study. The radii are expressed in Bohr.

Reference		Mo $4d^5 5s^1 5p^0 4f^0$	W $5d^4 6s^2 6p^0 5f^0$	O $2s^2 2p^4 3d^0 4f^0$	C $2s^2 2p^2 3d^0 4f^0$	H $1s^1 2p^0 3d^0 4f^0$
Core radius	s	2.75	2.45	1.47	1.56	1.33
	p	2.89	2.45	1.47	1.56	1.33
	d	2.49	2.45	1.47	1.56	0.37
	f	2.49	2.45	1.47	1.56	1.33

In this work, we focus on the transport property of Lindqvist Mo- and W-POM, the most common and stable members of the metal–oxygen clusters and POM families [39].

2. Computational procedures

The electronic structure and the geometrical configuration of $[M_6O_{19}]^{2-}$ (M = Mo, W) isolated molecules (Fig. 1) and $[M_6O_{19}]^{2-}$-based molecular junction (Scheme 1) have been calculated with the DFT code SIESTA [40–42] and benchmarked against previously published results [43].

For the isolated $[M_6O_{19}]^{2-}$ (M = Mo, W) molecules we build a large cubic supercell with a side 25 Å long in order to prevent the spurious interactions between the period images of the molecules. Norm-conserving pseudo-potentials are chosen to account for the core electrons [44], while the wave-functions of the valence ones are expanded over a numerical localized orbital basis set. The pseudopotential reference configuration and cutoff radii for each angular momentum shell of the atoms forming the molecules can be found in Table 1. Our pseudopotentials have been tested by comparing the eigenvalues of the isolated atoms with those calculated with all electron DFT. We have found extremely good agreement between the two calculations, with the largest energy error been smaller than 0.008 Ry. A double zeta plus polarization (DZP) basis is adopted for Mo, W, and O, while for H and C we reduce it to a single zeta plus polarization (SZP) one. An energy shift parameter of 0.02 Ry sets the cutoff radii of the radial part of the basis functions, while the real space grid, used to calculate some of the matrix elements, has an equivalent cutoff of 250 Ry. All the structures are fully optimized by conjugate gradient without any symmetry constraint until the forces acting on each atom are smaller than 0.02 eV/Å. Structural relaxation has been carried with both the local density approximation (LDA) of the DFT exchange and correlation functional parameterized by Ceperley and Alder, and the generalized gradient approximation (GGA) parameterized by Perdew, Burke, and Ernzerhof. Transport calculations have been performed only at the GGA level.

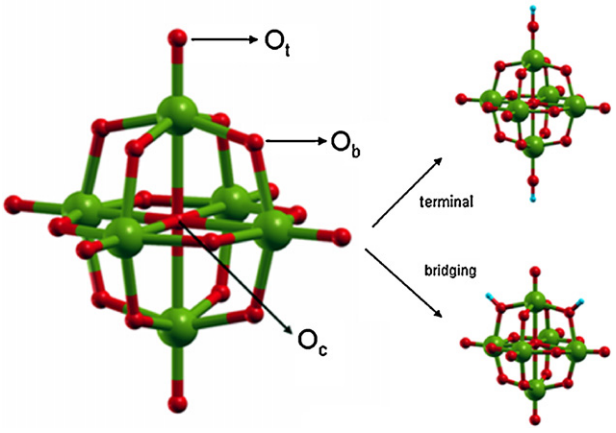

Fig. 1. Ball-stick representations of the Lindqvist anion $[M_6O_{19}]^{2-}$ (M = Mo, W) (color code: metal, green; oxygen, red; hydrogen, blue). In the right-hand side panels we show two different protonation models. (For interpretation of the references to color in this figure legend, the reader is referred to the web version of the article.)

The device structure explored in this work is shown in Scheme 1. We sandwich the $H_2M_6O_{19}$ (M = Mo, W) molecules between the two semi-infinite metallic armchair (5,5) carbon nanotubes (CNTs) in a scanning tunneling microscopy (STM) like geometry, where the two CNTs are both terminated by a half C_{60} cap [45]. Although the $H_2M_6O_{19}$ (M = Mo, W) and these capped CNTs have appreciable stability on their own, we perform additional structural optimization to include any conformation changes due to the proximity of the two systems and to the electrode–molecule interaction. The search for the optimal geometry is carried out as following. First, we bind directly the $H_2M_6O_{19}$ (M = Mo, W) molecule to the electrodes via the terminal oxygen atoms. Then, in order to obtain the lower energy molecular junction structure, we perform total energy DFT calculations at different electrode–electrode separations, with a resolution of 0.1 Å. At the energy minimum we then optimize the entire structure without any symmetry constraint by conjugate gradients until the largest atomic force is smaller than 0.04 eV/Å.

The SMEAGOL code [17,46,47], which is capable of studying large-scale two-terminal devices at DFT + NEGF level, is adopted to investigate the electron transport properties of such devices. SMEAGOL uses SIESTA as DFT platform, so that the same pseudopotentials, basis set and exchange and correlation functional of the structural calculations are adopted for the transport. The transmission coefficient, $T(E, V_b)$, calculated at the energy, E, and the bias voltage, V_b, is evaluated as

$$T(E, V_b) = Tr[\Gamma_L(E) G^R(E) \Gamma_R(E) G^A(E)] \quad (1)$$

where $G^R(E)$ and $G^A(E)$ are respectively the retarded and advanced Green's function of the central scattering region, Γ_L and Γ_R are the contact broadening functions (sometimes called the coupling matrix) associated to the left- and right-hand side electrodes, respectively. The current through the atomic scale system is then calculated with the Landauer–Büttiker formula [9],

$$I = \frac{2e}{h} \int T(E, V_b)[f_L(E - \mu_L) - f_R(E - \mu_R)]\mathrm{d}E \quad (2)$$

where f_L and f_R are the Fermi–Dirac distribution functions of the left and right electrodes with the electrochemical potentials μ, respectively. The applied bias voltage is introduced as a relative shift of the two electrodes chemical potentials namely, $e \cdot V_b = \mu_L - \mu_R$. For the system at equilibrium, the linear response conductance, G, is evaluated from the transmission coefficients $T(E)$ at the Fermi energy E_F, i.e., $G = G_0 \cdot T(E)$, where $G_0 = 2e^2/h$ is the fundamental quantum conductance unit. One of the advantages of the SMEAGOL scheme is that the evaluation of the surface Green's function is obtained by using a semi-analytical expression, which results in a largely enhanced algorithm stability [10,47]. The charge density is integrated over 40 energy point along the semi-circle, 20 energy points along the line in the complex plane and 20 poles in the Fermi distribution with 300 K electronic temperature. More details about the method and the particular implementation of SMEAGOL can be found in the literatures [10,17,46,47].

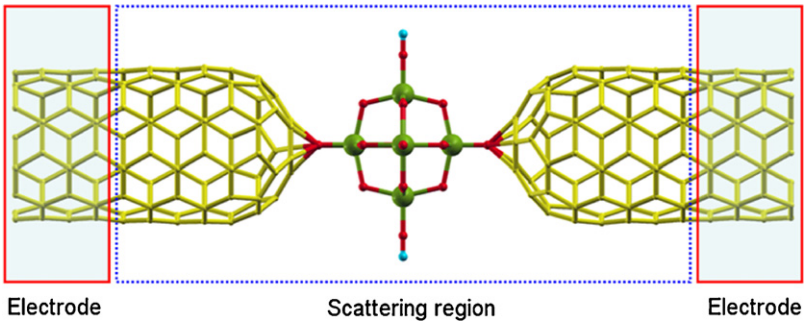

Scheme 1. The prototype device used in this work, in which a $H_2M_6O_{19}$ (M = Mo or W) molecule is sandwiched between two C_{60}-caped (5,5) CNTs (color code: metal, green; oxygen, red; carbon, yellow; hydrogen, blue). The region enclosed in the dashed box (blue) corresponds to the scattering region. (For interpretation of the references to color in this scheme legend, the reader is referred to the web version of the article.)

3. Results and discussion

3.1. The geometry of $[M_6O_{19}]^{2-}$ (M = Mo, W)

The main structural parameters of the $[M_6O_{19}]^{2-}$ (M = Mo, W) molecules (see Fig. 1) are summarized in Table 2 alongside with the experimental data for comparison. These latter have been taken from the average bond-lengths observed in the crystalline O_h phase [48]. As shown in the table, the optimized LDA bond-lengths are predicted to be slightly shorter than the experimental ones for Mo, while they are almost identical to the experiments for W. When the same are calculated with GGA we observe, as usual, a small increase in the bond-lengths, which nevertheless remain within 2% of the experimental values for both Mo and W. This is in good agreement with previous calculations for the same molecules [43]. As in standard calculations for the electronic transport usually LDA and GGA yield rather similar results, we have decided here to perform SMEAGOL calculations only at the GGA level.

3.2. Effect of the protonation over the electron transport

Due to the cationic nature of POMs in an actual experimental situation the single crystals are stabilized by counter ions interacting with the molecules via vdW forces. For convenience here we replace the counterions with passivating H ions so that the entire molecular device remains charge neutral. It is worth noting that in general in experiments it is difficult to determine the actual location of the protons around the POM anions thus that the progress of H protonation is complicate especially for a multistep protonation. Given these uncertainties we made some simplifications and just look at a number of different situations (see Fig. 1), in which the introduction of H produces minimal changes in the POM structure and does not affect its electronic configuration. For Keggin POMs, it has been established both experimentally and by DFT calculations [49–52] that the preferential protonation site is the bridge site. For the sake of simplicity here we have considered only two possible protonation geometries, namely when the H attached either to two bridging or to terminating sites (see Fig. 1).

It is apparent that the H protonated at the terminal oxygen site has minimal effects on the structure of $[M_6O_{19}]^{2-}$ (M = Mo, W). In this aspect, by adopting the terminal situation, not only the main structure of $[M_6O_{19}]^{2-}$ is preserved, but also the intriguing electronic property of $[M_6O_{19}]^{2-}$ are largely unaffected.

In general $[Mo_6O_{19}]^{2-}$ and $[W_6O_{19}]^{2-}$ have a rather similar electronic structure. Therefore, it is instructive to begin with $H_2Mo_6O_{19}$ and consider two protonation geometries with the aim of understanding the role of the protonation on the transport of this class of molecules. In Fig. 2 we present the zero-bias transmission coefficient as a function of energy for the two protonation models introduced in Fig. 1. From the figure one can note that the main effect of moving H from the terminating to the bridge site is that of shifting the upper part of the transmission spectrum (corresponding to the unoccupied states) down in energy by about 0.1–0.2 eV. In both cases however the Fermi level remains stably in the gap between the highest occupied molecular orbital (HOMO) and the lowest unoccupied molecular orbital (LUMO), so that the transport is via electron tunneling (see also Fig. 4b where the transmission coefficient is compared with the molecule density of states). Going into more details the first transmission peak above the Fermi level is almost halved when going from the bridge to the terminating site, while the triple peak structure below E_F found for the terminating side is replaced by a double peak at slighter lower energy for the bridge protonation geometry.

Table 2
Selected bond lengths for $[M_6O_{19}]^{2-}$ (M = Mo, W) as optimized with SIESTA. The experimental data reported here correspond to the average of crystal data based on O_h symmetry. The bond length unit in Å.

		GGA	LDA	Exp.
$[Mo_6O_{19}]^{2-}$	Mo-O_t	1.692	1.670	1.676
	Mo-O_b	1.933	1.904	1.928
	Mo-O_c	2.331	2.303	2.319
$[W_6O_{19}]^{2-}$	W-O_t	1.739	1.695	1.693
	W-O_b	1.974	1.916	1.924
	W-O_c	2.388	2.328	2.325

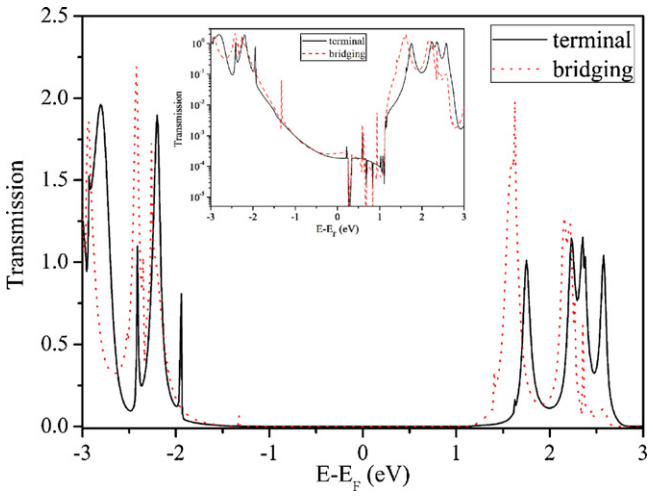

Fig. 2. Zero-bias transmission coefficient as a function of energy for $H_2Mo_6O_{19}$. In the insert the same quantity is plotted on a logarithmic scale. The Fermi level, E_F, has been set to zero.

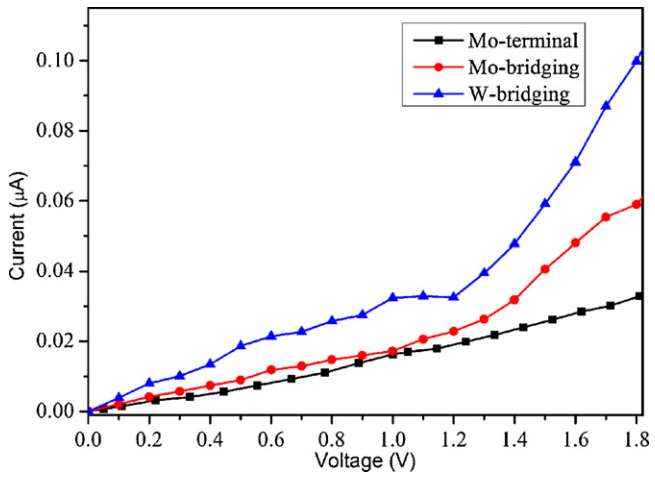

Fig. 3. Current–voltage, *I–V*, characteristic for devices comprising a $H_2M_6O_{19}$ molecule (M = Mo, W) sandwiched between CNTs electrodes. In the case of Mo we consider two protonation geometries.

Such transmission spectra translate in the corresponding current–voltage, *I–V*, curves, which are shown next in Fig. 3. In the figure we report only the positive bias region since the molecule is symmetric so that the following relation holds $I(-V) = -I(V)$. From the figure we can note a rather smooth and generally featureless *I–V* characteristic. Note in particular that there is no steep increase in the current at any voltage in the range investigated. This is expected as the first peak in $T(E)$ appears only at about 1.2 eV above E_F, i.e., it is expected to contribute to the current only for $V_b > 2.4$ V.

We then conclude this section by noting that the role of protonation is only minor in determining the transport properties of the $H_2M_6O_{19}$ molecule, that is both the *I–V* curve and the transmission profile are little sensitive to the precise position of the passivating H ion. Given this insensitivity to the geometry we conclude that our calculated *I–V* can be a good approximation of the same obtained for a molecule embedded in a crystal, where the role of the H is replaced by appropriate counterions.

3.3. Comparing the transport property of Mo and W based $H_2M_6O_{19}$

Given the close structural and electronic parameters of Mo and W based $[M_6O_{19}]^{2-}$ (M = Mo, W) molecules we now compare their transport properties. The model device for $H_2W_6O_{19}$ is constructed from that of $H_2Mo_6O_{19}$ by simply replacing Mo with W and then by performing further geometrical relaxation. In the calculations involving $H_2W_6O_{19}$ we use identical exchange and correlation functional and convergence parameters than those used for $H_2Mo_6O_{19}$.

In Fig. 4a, we plot the zero-bias transmission coefficient on a linear scale for both the $H_2W_6O_{19}$ and $H_2Mo_6O_{19}$ molecule. In particular we consider the geometries where the protonation occurs at the O bridging sites only (see Fig. 1). In general, the transmission profile for $H_2W_6O_{19}$ and $H_2Mo_6O_{19}$ are remarkably similar, with the electrodes' Fermi level well placed in the HOMO–LUMO gap and the transport dominated by tunneling. Intriguingly, in contrast to the calculated HOMO–LUMO gap for the molecules in the gas phase (3 eV for $[W_6O_{19}]^{2-}$ and 2.6 eV for $[Mo_6O_{19}]^{2-}$), the transport HOMO–LUMO gap (defined as the energy separation between the first transmission peak respectively for the occupied and empty states) is smaller for $H_2W_6O_{19}$. Such a difference is essentially attributed to the slightly higher position of the tail of the first transmission peak below the Fermi level of $H_2W_6O_{19}$ with respect to that of $H_2Mo_6O_{19}$. In contrast, the transmission coefficient for energies

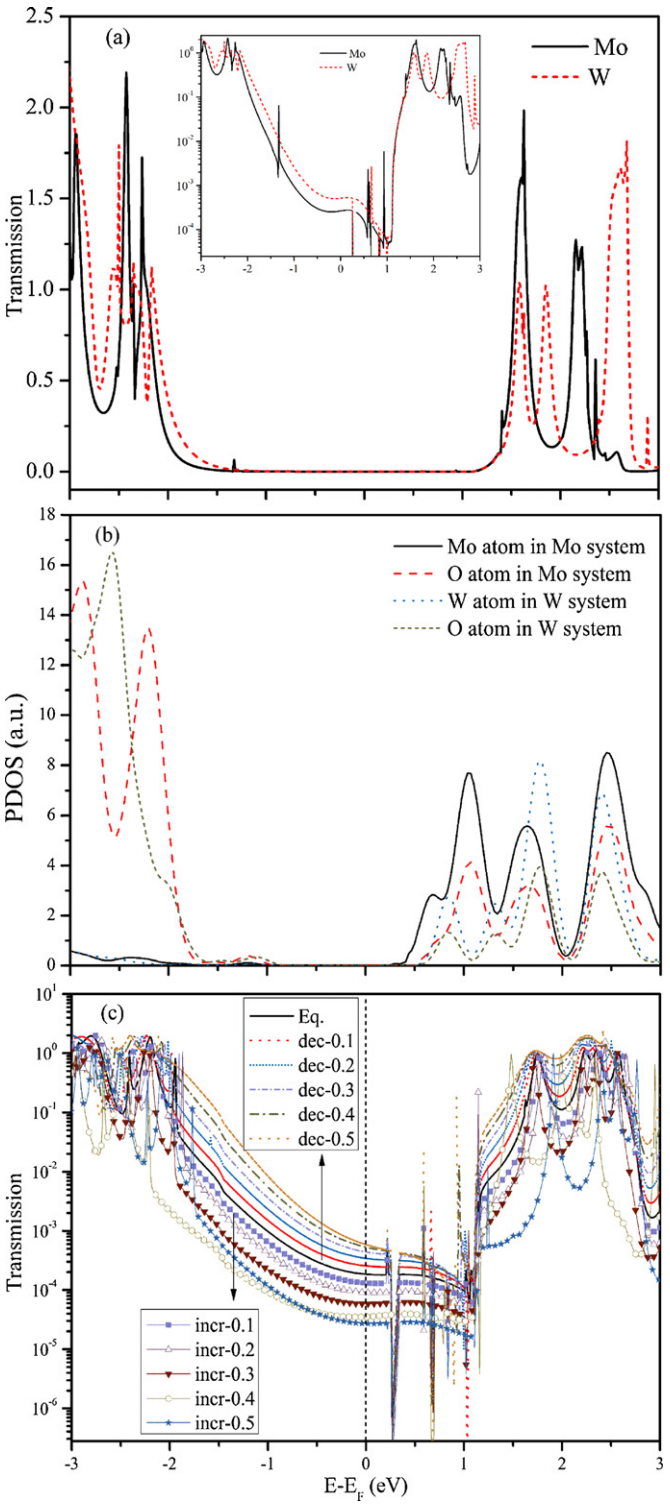

Fig. 4. (a) Transmission spectrum of the $H_2W_6O_{19}$ and $H_2Mo_6O_{19}$ molecules sandwiched between two CNTs. Here the molecules are protonated at the bridging sites and the transmission is calculated at zero-bias. (b) The partial (atom resolved) DOS of the $H_2W_6O_{19}$ and $H_2Mo_6O_{19}$ molecules sandwiched in a CNT–$H_2M_6O_{19}$–CNT junction. The DOS smearing is 0.15 eV. (c) Distance-dependent zero-bias transmission spectrum for $H_2Mo_6O_{19}$. Here 'dec' ('incr') means that the molecule/electrode distance has been decreased (increased) by multiples of 0.1 Å with respect to the GGA equilibrium distance.

above E_F follows the same slope for the two molecules, i.e., it sharply increases at $E - E_F \sim 1.5$ eV.

A deeper understanding of the transmission process can be achieved by looking at the orbital resolved density of states presented in Fig. 4b. We note that the HOMO of both the molecules is characterized by a strong O contribution, while the LUMO receives contributions also from the metallic centers. Most importantly for the discussion the main O peak in the HOMO is lower for $H_2W_6O_{19}$ than for $H_2Mo_6O_{19}$, thus confirming the fact that the molecule HOMO–LUMO gap is larger for $H_2W_6O_{19}$. However we also note a small shoulder in the HOMO DOS at energies larger than the main HOMO (between −1.5 eV and −1 eV below E_F). This originates from the interaction between the molecules and the electrodes, which lowers the molecule symmetry (from O_h to D_{4h} with protonation and then to D_{2h} because of the electrodes), and provides additional DOS for the transport. As such the onset of the transmission near the HOMO is driven by this molecule/electrode hybrid state. Its efficiency to conduct electrons depends on the strength of the interaction, which ultimately is associated to the distance between the molecule and the electrodes. Hence, since $H_2W_6O_{19}$ is slightly larger than $H_2Mo_6O_{19}$, we expect higher conductance associated to such a hybrid state for $H_2W_6O_{19}$, as proved by our calculated transmission coefficient.

Such a hypothesis is confirmed by a number of test calculations for $H_2Mo_6O_{19}$, where we artificially vary the molecule-CNT distance in steps of 0.1 Å, while keeping the molecule geometry rigid. The transmission spectrum is shown in Fig. 4c. With decreasing the molecule–electrode distance the conductance is stably increased, while an enhancement of such a distance results in a lower conductance. In particular we note that the onset of transmission at the LUMO is left unchanged by varying the molecule/electrode distance, as expected from a transport process occurring through a molecular level associated to the central metal. In contrast at the HOMO edge the transmission progressively increases as a result of the enhanced hybridization.

The transmission features discussed above map directly onto the *I*–*V* curves, which are shown in Fig. 3 for both $H_2W_6O_{19}$ and $H_2Mo_6O_{19}$. As expected, the $H_2W_6O_{19}$-based junction presents a higher current for all the voltages investigated, although the general features of the *I*–*V* curves are rather similar for the two molecules. In particular we note a rather linear slope, at least up to the voltages investigated. We can then conclude that both the molecules transmit electrons through a tunneling mechanism for a rather wide bias range. As the first large conductance peak in the transmission is for the LUMO and it is at least 1 eV away from the Fermi level, we do not expect resonant transport through a molecular level, at least up to voltages of 2 V. Note that this indeed can be an underestimation as the GGA HOMO–LUMO is usually significantly smaller than the real one.

4. Conclusions

In the present work we report a first study of Lindqvist polyoxometalates (Mo and W) based molecular junctions by using the DFT + NEGF method. We find that protonation weakly affects the transport properties, which are also similar for both Mo- and W-based complexes. In particular the transmission at the Fermi level is dominated by a tunneling mechanism with the first of the molecular levels available for resonant transport being at least 1 eV away from E_F. This means that such junctions can sustain a tunneling current for voltages at least up to 2 V, as confirmed by our calculated *I*–*V* curves. Such electronic and transport properties, combined with the significant structural stability of Lindqvist polyoxometalates, suggest that this class of molecules may be employed in high-voltage applications.

Acknowledgments

The authors gratefully acknowledge financial support from NSFC (20971020, 21073030, and 21131001), Doctoral Fund of Ministry of Education of China (20100043120007), and the Science and Technology Development Planning of Jilin Province (20100104). The Smeagol project (SS) is sponsored by Science Foundation of Ireland (grants 07/IN.1/I945) and by CRANN.

References

[1] A. Aviram, M.A. Ratner, Molecular rectifiers, Chemical Physics Letters 29 (1974) 277–283.
[2] M.A. Reed, C. Zhou, C.J. Muller, T.P. Burgin, J.M. Tour, Conductance of a molecular junction, Science 278 (1997) 252–254.
[3] H. Ohnishi, Y. Kondo, K. Takayanagi, Quantized conductance through individual rows of suspended gold atoms, Nature 395 (1998) 780–783.
[4] J. Chen, M.A. Reed, A.M. Rawlett, J.M. Tour, Large on–off ratios and negative differential resistance in a molecular electronic device, Science 286 (1999) 1550–1552.
[5] J.M. Tour, A.M. Rawlett, M. Kozaki, Y. Yao, R.C. Jagessar, S.M. Dirk, D.W. Price, M.A. Reed, C.W. Zhou, J. Chen, W. Wang, I. Campbell, Synthesis and preliminary testing of molecular wires and devices, Chemistry: A European Journal 7 (2001) 5118–5134.
[6] A. Nitzan, M.A. Ratner, Electron transport in molecular wire junctions, Science 300 (2003) 1384–1389.
[7] B.Q. Xu, N.J.J. Tao, Measurement of single-molecule resistance by repeated formation of molecular junctions, Science 301 (2003) 1221–1223.
[8] L. Venkataraman, J.E. Klare, C. Nuckolls, M.S. Hybertsen, M.L. Steigerwald, Dependence of single-molecule junction conductance on molecular conformation, Nature 442 (2006) 904–907.
[9] S. Datta, Electronic Transport in Mesoscopic Systems, Cambridge University Press, Cambridge, 1995.
[10] S. Sanvito, C.J. Lambert, J.H. Jefferson, A.M. Bratkovsky, General Green's-function formalism for transport calculations with spd Hamiltonians and giant magnetoresistance in Co- and Ni-based magnetic multilayers, Physical Review B 59 (1999) 11936.
[11] Y.Q. Xue, S. Datta, M.A. Ratner, Charge transfer and "band lineup" in molecular electronic devices: a chemical and numerical interpretation, Journal of Chemical Physics 115 (2001) 4292–4299.
[12] J. Taylor, H. Guo, J. Wang, Ab initio modeling of quantum transport properties of molecular electronic devices, Physical Review B 63 (2001) 245407.
[13] Y.Q. Xue, S. Datta, M.A. Ratner, First-principles based matrix Green's function approach to molecular electronic devices: general formalism, Chemical Physics 281 (2002) 151–170.
[14] M. Brandbyge, J.L. Mozos, P. Ordejón, J. Taylor, K. Stokbro, Density-functional method for nonequilibrium electron transport, Physical Review B 65 (2002) 165401.
[15] S.H. Ke, H.U. Baranger, W.T. Yang, Electron transport through molecules: self-consistent and non-self-consistent approaches, Physical Review B 70 (2004) 085410.
[16] K.S. Thygesen, K.W. Jacobsen, Molecular transport calculations with Wannier functions, Chemical Physics 319 (2005) 111–125.
[17] A.R. Rocha, V.M. García-Suárez, S. Bailey, C. Lambert, J. Ferrer, S. Sanvito, Spin and molecular electronics in atomically generated orbital landscapes, Physical Review B 73 (2006) 085414.
[18] Y.-H. Kim, J. Tahir-Kheli, P. Schultz, W.A. Goddard III, First-principles approach to the charge-transport characteristics of monolayer molecular-electronics devices: application to hexanedithiolate devices, Physical Review B 73 (2006) 235419.
[19] G. Stefanucci, C.O. Almbladh, Time-dependent quantum transport: an exact formulation based on TDDFT, Europhysics Letters 67 (2004) 14–20.
[20] G. Stefanucci, C.O. Almbladh, Time-dependent partition-free approach in resonant tunneling systems, Physical Review B 69 (2004), 195318-195311–195318-195317.
[21] S. Kurth, G. Stefanucci, C.O. Almbladh, A. Rubio, E.K.U. Gross, Time-dependent quantum transport: a practical scheme using density functional theory, Physical Review B 72 (2005) 035308.
[22] X. Zheng, G.-H. Chen, First-Principles Method for Open Electronic Systems, 2005 arXiv:physics/0502021v1.
[23] G. Stefanucci, C.O. Almbladh, An exact ab initio theory of quantum transport using TDDFT and nonequilibrium Green's functions, Journal of Physics: Conference Series 35 (2006) 17–24.
[24] J. Gabelli, G. Fève, J.M. Berroir, B. Plaçais, A. Cavanna, B. Etienne, Y. Jin, D.C. Glattli, Violation of Kirchhoff's laws for a coherent RC circuit, Science 313 (2006) 499–502.
[25] X. Zheng, F. Wang, C. Yam, Y. Mo, G. Chen, Time-dependent density-functional theory for open systems, Physical Review B 75 (2007) 195127.
[26] J. Yuen-Zhou, D.G. Tempel, C.a. Rodríguez-Rosario, A. Aspuru-Guzik, Time-dependent density functional theory for open quantum systems with unitary propagation, Physical Review Letters 104 (2010) 043001.

[27] X. Zheng, G. Chen, Y. Mo, S. Koo, H. Tian, C. Yam, Y. Yan, Time-dependent density functional theory for quantum transport, Journal of Chemical Physics 133 (2010) 114101.
[28] S. Wen, S. Koo, C. Yam, X. Zheng, Y. Yan, Z. Su, K. Fan, L. Cao, W. Wang, G. Chen, Time-dependent current distributions of a two-terminal carbon nanotube-based electronic device, Journal of Physical Chemistry B 115 (2011) 5519–5525.
[29] M.T. Pope, in: A.G. Wed (Ed.), Comprehensive Coordination Chemistry II, Oxford, UK, 2004.
[30] E. Kapetanakis, A.M. Douvas, D. Velessiotis, E. Makarona, P. Argitis, N. Glezos, P. Normand, Hybrid organic–inorganic materials for molecular proton memory devices, Organic Electronics 10 (2009) 711–718.
[31] D.E. Katsoulis, A survey of applications of polyoxometalates, Chemical Reviews 98 (1998) 359–387.
[32] E. Kapetanakis, A.M. Douvas, D. Velessiotis, E. Makarona, P. Argitis, N. Glezos, P. Normand, Molecular storage elements for proton memory devices, Advanced Materials 20 (2008) 4568–4574.
[33] E. Coronado, C. Gimenezsaiz, C. Gomezgarcia, Recent advances in polyoxometalate-containing molecular conductors, Coordination Chemistry Reviews 249 (2005) 1776–1796.
[34] M.T. Pope, A. Müller, Polyoxometalate chemistry: an old field with new dimensions in several disciplines, Angewandte Chemie International Edition 30 (1991) 34–48.
[35] N. Glezos, P. Argitis, D. Velessiotis, C.D. Diakoumakos, Tunneling transport in polyoxometalate based composite materials, Applied Physics Letters 83 (2003) 488–490.
[36] N. Glezos, D. Velessiotis, G. Chaidogiannos, P. Argitis, D. Tsamakis, X. Zianni, Transport properties of polyoxometalate containing polymeric materials, Synthetic Metals 138 (2003) 267–269.
[37] G. Chaidogiannos, D. Velessiotis, P. Argitis, P. Koutsolelos, C.D. Diakoumakos, D. Tsamakis, N. Glezos, Tunneling and negative resistance effects for composite materials containing polyoxometalate molecules, Microelectronic Engineering 73–74 (2004) 746–751.
[38] D. Velessiotis, N. Glezos, V. Ioannou-Sougleridis, Tungstate polyoxometalates as active components of molecular devices, Journal of Applied Physics 98 (2005) 084503.
[39] T. He, J. He, M. Lu, B. Chen, H. Pang, W.F. Reus, W.M. Nolte, D.P. Nackashi, P.D. Franzon, J.M. Tour, Controlled modulation of conductance in silicon devices by molecular monolayers, Journal of the American Chemical Society 128 (2006) 14537–14541.
[40] P. Ordejón, E. Artacho, J. Soler, Self-consistent order-N density-functional calculations for very large systems, Physical Review B 53 (1996) R10441–R10444.
[41] D. Sánchez-Portal, P. Ordejón, E. Artacho, J.M. Soler, Density-functional method for very large systems with LCAO basis sets, International Journal of Quantum Chemistry 65 (1997) 453–461.
[42] J.M. Soler, E. Artacho, J.D. Gale, A. García, J. Junquera, P. Ordejón, D. Sánchez-Portal, The SIESTA method for ab initio order-N materials, Journal of Physics: Condensed Matter 14 (2002) 2745–2779.
[43] J. Li, Electronic structures (d–π) conjugation effects, and spectroscopic properties of polyoxometalates: $M_6O_{19}^{2-}$ (M = Cr, Mo, W), Journal of Cluster Science 13 (2002) 137–163.
[44] N. Troullier, J.L. Martins, Efficient pseudopotentials for plane-wave calculations. II: operators for fast iterative diagonalization, Physical Review B 43 (1991) 8861–8869.
[45] K.H. Khoo, J.B. Neaton, Y.W. Son, M.L. Cohen, S.G. Louie, Negative differential resistance in carbon atomic wire-carbon nanotube junctions, Nano Letters 8 (2008) 2900–2905.
[46] A.R. Rocha, V. Garcia-Suarez, S.W. Bailey, C.J. Lambert, J. Ferrer, S. Stefano, Towards molecular spintronics, Nature Materials 4 (2005) 335–339.
[47] I. Rungger, S. Sanvito, Algorithm for the construction of self-energies for electronic transport calculations based on singularity elimination and singular value decomposition, Physical Review B 78 (2008) 035407.
[48] H.R. Allcock, E.C. Bissell, E.T. Shawl, Crystal and molecular structure of a new hexamolybdate–cyclophosphazene complex, Inorganic Chemistry 12 (1973) 2963–2968.
[49] X. López, C. Bo, J.M. Poblet, Electronic properties of polyoxometalates: electron and proton affinity of mixed-addenda Keggin and Wells–Dawson anions, Journal of the American Chemical Society 124 (2002) 12574–12582.
[50] S. Ganapathy, M. Fournier, J.F. Paul, L. Delevoye, M. Guelton, J.P. Amoureux, Location of protons in anhydrous Keggin heteropolyacids $H_3PMo_{12}O_{40}$ and $H_3PW_{12}O_{40}$ by $^1H\{^{31}P\}/^{31}P\{^1H\}$ REDOR NMR and DFT quantum chemical calculations, Journal of the American Chemical Society 124 (2002) 7821–7828.
[51] W. Guan, L. Yan, Z. Su, S. Liu, M. Zhang, X. Wang, Electronic properties and stability of dititanium(IV) substituted alpha-Keggin polyoxotungstate with heteroatom phosphorus by DFT, Inorganic Chemistry 44 (2005) 100–107.
[52] W. Guan, L. Yan, Z. Su, E. Wang, X. Wang, Density functional study of protonation sites of a-Keggin isopolyanions, International Journal of Quantum Chemistry 106 (2006) 1860–1864.